X-Band EPR Spectrometer with Customizable Arbitrary Waveform Generator based on a 1 GHz DAC Board

Thomas Kaufmann[1], John M. Franck[1], Timothy J. Keller[1], Ryan P. Barnes[1], Steffen J. Glaser[2],John M. Martinis[3], Songi Han[1,4*]

[1]Department of Chemistry and Biochemistry, University of California Santa Barbara, Santa Barbara, CA
[2]Department of Chemistry, TechnischeUniversitätMünchen, Germany
[3]Department of Physics, University of California Santa Barbara, Santa Barbara, CA
[4]Department of Chemical Engineering, University of California Santa Barbara, Santa Barbara, CA

* = corresponding author, Songi Han, Department of Chemistry and Biochemistry 9510, University of California Santa Barbara, CA, USA, Phone: +1 (805) 893-4858, Fax: +1 (805) 893-4120 , Email: songi@chem.ucsb.edu

Abstract

We present an EPR spectrometer featuring an arbitrary waveform generator (AWG) operating at 8–10 GHz (X-band) that is based on a 1 GHz digital-to-analog converter (DAC) boardwith a 42 dB (i.e. 14-bit) dynamic range. This AWG-capable spectrometer was developedto widen the scope of pulsed electron paramagnetic resonance (EPR) and enable new experiments. It generates shaped X-band pulses with precise amplitude and phase control and can specify inter-pulse delays with a time resolution of ≤250 ps. We demonstrate the capabilities of the spectrometer by presenting spin-echo measurements that implement an entirely digitally controlled and calibrated 16-step phase cycle and by measuring the excitation profiles seen by the spins in the microwave resonator as they respond to various pulse shapes, including rectangular, triangular, Gaussian, sinc, and adiabatic rapid passage waveforms. Potential applications of these capabilities, and their implementation in commercial instrumentation, will be discussed.

1. Introduction

Pulsed electron paramagnetic resonance (EPR) probes the local environment of paramagnetic species – most commonly, stablenitroxide radicals – that are attached as "spin labels" to biomolecular surfaces. After the strategic labeling of one or two sites, pulsed EPR can reveal information about closely coupled nuclei, inter-spin label distances of between 2 and 8 nm, local side-chain flexibility, or conformational exchange dynamics.[1] The most widely available pulsed EPR instruments operate at 8-10 GHz (X-band) and rely on Gunn diode or klystron microwave sources together with traveling wave tube amplifiers. Such instruments generate rectangular shaped $\sim$0.5 – 1 kW pulses, whose phase and amplitude must be chosen from a list of typically only 4 values, corresponding to the number of "channels" on the spectrometer. Despite their already enormous potential, even the most state of the

art pulsed X-band EPR instrument available today has clearly not yet reached technological maturity and, thus, offers much room for enhanced performance and versatility.

Typically, pulsed X-band EPR performance suffers from insufficient excitation bandwidths that cannot fully excite the EPR spectra of spin-labeled macromolecules, which span several hundred MHz.[2] The ability to not only broadly, but also uniformly, excite different portions of the spectrum to probe their interactions and/or distances would – in particular – benefit two-dimensional (2D) EPR experiments. These include double electron-electron resonance (DEER),[3,4] which has a prominent and growing importance throughout biochemistry, as well as electron double resonance (ELDOR) experiments,[5] which have proven particularly useful for probing questions about the interactions between proteins and lipid membranes and may offer insight into the formation of lipid rafts – among others.[6,7] Broader excitation bandwidths can be achieved with one of two strategies: the implementation of higher power rectangular excitation pulses or the implementation of shaped microwave pulses whose amplitude and phase is strategically modulated at a ns resolution.

A series of advances in NMR over the past 30 years encourage us to pursue the latter strategy. In particular, it has been shown that arbitrarily shaped pulses can excite spins over a wider bandwidth than is possible with rectangular pulses of the same power, can provide highly uniform excitation profiles across a wide range of frequency offsets,[8] can excite sharper spectral slices,[9] and can permit dramatic levels of control over even coupled spin systems.[10] In fact, it could be said that pulse shaping has induced a paradigm shift in NMR. Similarly, shaped pulses in EPR should enable excitation of sharper and wider spectral slices, offer significant improvements to the sensitivity and accuracy of DEER-based distance measurements, and reduce the detector dead-time – to name just a few of many potential applications. However, to date, while composite pulses,[11] stochastic excitation,[12] and tailored pulses[13] have been utilized in EPR, only very few spectrometers feature arbitrary waveform generation (AWG) capabilities in the X-band (8-12 GHz) frequency regime.[14]Notable recent developments in this direction include two very recent and interesting applications of control algorithms pertaining to long-lived systems and targeted for quantum computation applications[15,16], the all-digital pulsed EPR spectrometer developed by Tseitlin et.al.[17]that was used in conjunction with a commercial AWG (Tektronix AWG7122C) at 256 MHz, 1 GHz, and 10 GHz, as well as the AWG capabilities implemented by Spindler et. al. at 10 GHz (AWG custom-designed by Innovative Technical Systems, Inc., AWG 8200)in conjunction with a commercial EPR spectrometer (Bruker ELEXSYS E580) to generate shaped pulses with a dramatically broadened excitation bandwidth.[14]

We present a home-built, stand-alone AWG X-band EPR spectrometer that is entirely controlled by and centered around a 1 GHz digital-to-analog converter (DAC) board. An yttrium iron garnet (YIG)-tuned oscillator and an amplifier

consisting of 4 parallel solid-state amplifier modules offer 12-13 W of microwave power at 9.1 – 10.9 GHz. The spectrometer fully controls the amplitude (42 dB dynamic range) and phase (0.007° resolution) of a waveform with 1 ns time resolution. This corresponds to the finest time-domain resolution useful to X-band spectroscopy, since even a resonator that is overcoupled to a Q of only 100 would only absorb frequencies over a bandwidth of ~100 MHz. Thus, the resonator bandwidth – rather than the 1 ns time resolution of the spectrometer – limits the time resolution of the waveform that reaches the spins through a convolution-broadening with the ~10 ns long impulse response of the resonator (when employing a cavity with a Q of 100). A Python-based programming platform controls the spectrometer and easily generates any arbitrarily shaped pulses. These can be entered into the pulse program either numerically – as could, in the future, be generated by optimization or feedback – or analytically – as is the case for the Gaussian, truncated sinc, and adiabatic pulses presented here. These pulses excite the spins within the microwave resonator in the expected fashion, as demonstrated by experiments that read out the response of the spins themselves. Furthermore, the software and hardware can adjust inter-pulse delays by increments of <250 ps and permit finely resolved spin-echo measurements of relaxation decays.
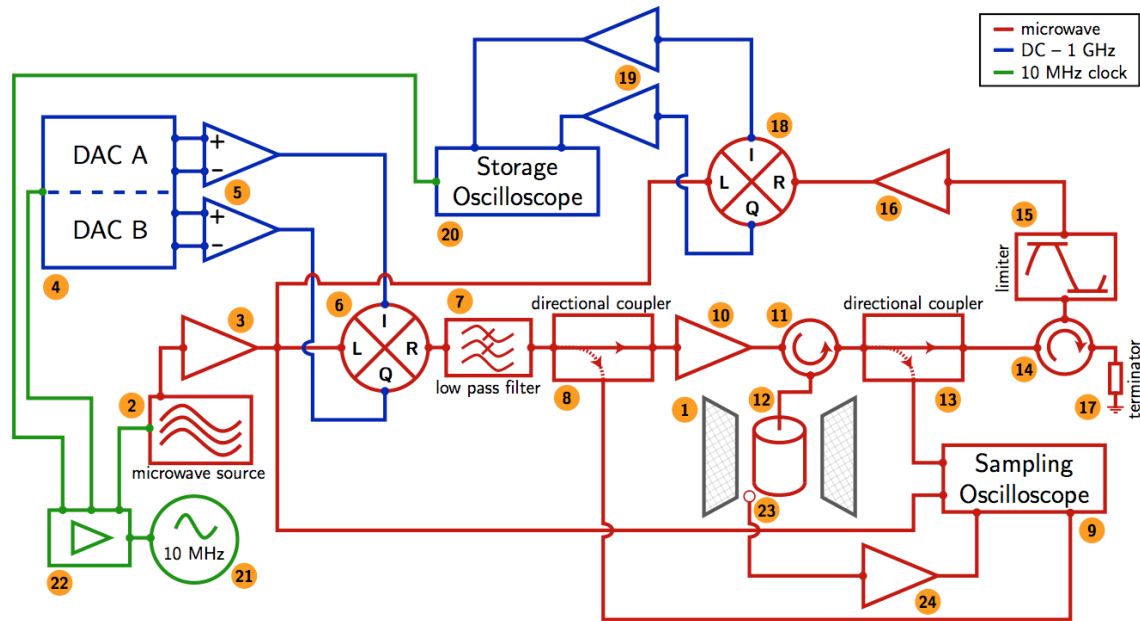
2. Experimental

2.1. Hardware

Fig. 1:Schematic overview of the pulsed AWG X-band EPR spectrometer.X-band microwave paths, indicated in red, transmit the pulse waveforms and carry the returning signal via coaxial cables, except for components #11, #13, #14, and #17, which are X-band waveguide

components. DC to 1 GHz signal paths are denoted in blue, and are present in both the AWG unit and the heterodyne detector. A 10 MHz reference signal is used to synchronize multiple components and is shown in green. The microwave carrier is generated (#2), amplified (#3), and mixed (#6) with two digitally controlled, quadrature 1 GHz transmit waveforms that are generated by the DAC board (#4) and amplified by two differential amplifiers (#5) to generate shaped X-band pulses at –10 dBm. The output waveform is filtered (#7), amplified to ~43 dBm (#10), and sent to the resonator (#12). The returning signal is power-limited (#15), and amplified (#16), before being sent to the heterodyne detector comprising an IQ mixer (#18) that generates two quadrature 1 GHz intermediate frequency (IF) waveforms, which are amplified (#19) and detected by the storage oscilloscope (#20). The 10 MHz reference oscillator (#21) is connected to a distribution amplifier (#22), which supplies the clock signal to the microwave source, DAC board, and detector. Appendix A describes the various labeled components in detail.

Component synchronization: Before tracing the path of the microwave signal to and from the detector, it is important to note that, in order to sensibly manipulate and detect waveforms with a ~1° accuracy in the microwave X-band phase, the system needs to consistently synchronize every hardware component that generates or detects any pulsed waveforms to within ~0.3 ps. Towards this end, an oven-controlled 10 MHz oscillator (Electronic Research Co. Model 130, Fig. 1 – #21) and a 10 MHz distribution amplifier (Stanford Research Systems Model FS735, Fig. 1 – #22) supply a 10 MHz clock signal. We chose a DAC board (High Speed Circuit Consultants, software build 10, Fig. 1 – #4), a digital storage oscilloscope (either Agilent Technologies MSO7104B or the digitizer card Agilent Acqiris 1082A, Fig. 1 – #20), and a YIG-tuned oscillator (MicroLambda MLSL-1178, Fig. 1 – #2) that can all synchronize to this clock signal via a phase-locked-loop (PLL) mechanisms.

Microwave source: The YIG-tuned oscillator (Fig. 1 – #2) outputs a phase-coherent microwave carrier between 8 and 10 GHz at 10 dBm. As described in Appendix A.1 the frequency output is computer-controlled.
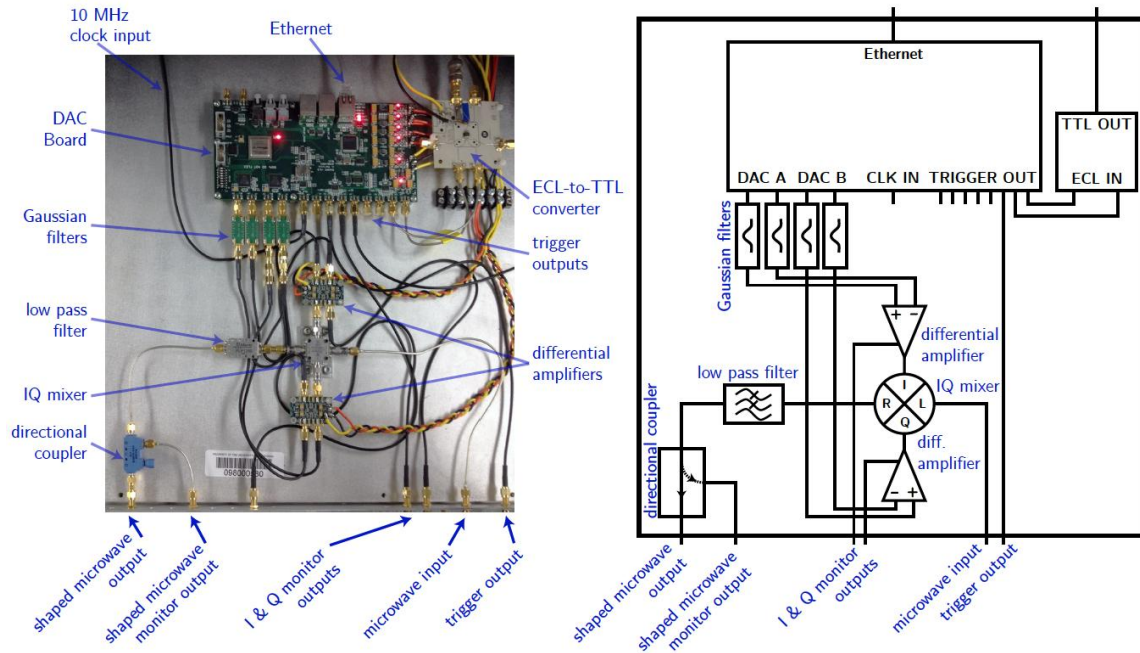
Fig. 2:Photograph and schematic of the arbitrary waveform generation (AWG) unit. The figure shows the 1 GHz digital-to-analog converter (DAC) board, Gaussian filters, differential amplifiers, IQ mixer, low pass filter, directional coupler, and ECL-to-TTL converter.

Arbitrary waveform generation at X-band: The X-band carrier wave next passes through a preamplifier (MiniCircuits ZX60-183+, Fig 1 – #3, Appendix A.1), reaching a power of 18 dBm, before passing through an IQ mixer (Marki Microwave IQ-0618 L XP, Fig. 1 – #6) that shapes the amplitude and phase of the microwave waveform with an output power of about –10 dBm. Among the important capabilities discussed in Appendix A.2, the central DAC board unit controls the voltage across the two quadrature IF (i.e. intermediate frequency) ports of the IQ mixer with 1 ns time resolution, i.e. a 1 GHz bandwidth, (see Fig. 1 – #4 and Fig. 2). Thus, the frequency profile of the waveform exiting the IQ mixer has an arbitrarily controlled profile in frequency space that spans ± 500 MHz from the frequency of the carrier wave. As a result, the spectrometer generates an X-band pulse sequence whose amplitude and phase are controlled with 1 ns time resolution. A notable and important feature, however, is that the timing between the pulses (as demonstrated and explained in the results section) can be altered by steps of ≤ 250 ps, i.e. finer than the time resolution of the X-band waveform. This is achieved by defining the desired waveform with arbitrary time resolution, given and subsequently employing the large dynamic range of the DAC board to down-sample to the native 1 ns resolution of the DAC board in such a way that the precise relative positions of the pulses are conserved.

Microwave amplifier, bridge, and resonator: Next, the arbitrarily shaped microwave pulses are pre-amplified by 24 dB (MiniCircuits ZX60-183+, Fig. 1 – #10)

and further amplified by a parallel array of solid-state amplifiers (Advanced Microwave PA2803-24, Fig. 1 – #10, Appendix A.3) to a peak amplitude of 12-13 W (41dBm), before travelling through a circulator (Cascade Research X-43-2, Fig. 1 – #11) into the microwave resonator (BrukerBioSpin ER4118X-MD5, Fig. 1 – #12). For all experiments here, the resonator was kept at room temperature in a static magnetic field of ~0.35 T (Fig. 1 – #1, Appendix A.1). The EPR signal, along with the resonator ringdown, passes out of the resonator and through a different port of the circulator (Fig. 1 – #11), which directs the signal towards the heterodyne detector (Fig. 1 – #14 to 20).

Heterodyne signal detection: The heterodyne detector (Fig. 1 – #14 to 20), which is a standard setup that was built based on the principles as presented in Rinard et al.,[18] digitizes the signal in quadrature, capturing it on an oscilloscope with 1 GHz bandwidth (Fig. 1 – #20).   More details are described in Appendix A.4.

Computer interface: The spectrometer is controlled entirely through the Python scripting language (see Appendix B.1). In-house Python libraries simplify the interaction and communication with the DAC board (Fig. 1 – #4), detection oscilloscope (Fig. 1 – #20), YIG-tuned oscillator (Fig. 1 – #2), and sampling oscilloscope (Fig. 1 – #9 used for calibration, as described in the next section) – these are connected to the computer through, respectively, Direct Ethernet, TCP/IP Ethernet, USB, and GPIB (converted to TCP/IP Ethernet with a GPIB-Ethernet Controller 1.2 by Prologix, LLC) connections.

As shown in Appendix B.2, the Python programming language allows us to specify a format for pulse programming that is both simple and versatile and that specifies both the shape of the microwave waveforms as well as the relative position of the various timing triggers sent to the detector oscilloscope or any gated amplifier (see Appendix B.2). As the results section will demonstrate, there is a distinct benefit in specifying the pulse sequence at an arbitrarily high resolution and allowing the pulse-programming back-end (i.e. the underlying in-house Python library) to automatically down-sample the result to 1 ns resolution (see Appendix C.1 for details). Furthermore, the pulse programming back-end automatically incorporates the results of various calibration procedures, as described next.

Calibration: The spectrometer, as described up to this point, has various imperfections. Imbalances in the DAC board output levels (see Fig. 2) and imbalances in the amplitude and phase characteristics of the transmit IQ mixer (Fig. 1 – #6) lead to systematic imperfections in the transmitted amplitude and phase of the waveforms, as well as a low-level bleed-through of the carrier wave. Furthermore, similar imbalances in the heterodyne detector's IQ mixer (Fig.1 – #18) and amplifiers (Fig. 1 – #19) can lead to imbalances in the quadrature detection channels that results in a DC offset, as well as amplitude and phase imbalance between the real and imaginary channel of the detected signal. Rather than pursuing the task of improving the performance of each of the relevant hardware components, which would be exceedingly difficult, we simply implement digital

calibration routines that correct for these imperfections, a strategy previously implemented by Martinis et. al.[19] in a different experimental setup following different calibration routines.

All such routines require knowledge of the exact amplitude and phase of the waveform output by the AWG (i.e. output from the transmitting IQ mixer, Fig. 1 – #6) as a starting reference point. To avoid introducing errors from the mixers, diodes, or amplifiers that constitute the home-built detector, we must record this waveform as directly as possible. To achieve this, we employ a sampling oscilloscope (Fig. 1 – #9), which acquires only one sample point per acquisition, but does so accurately, linearly, and with a very high (20 GHz) detection bandwidth. By providing a phase-coherent (i.e. consistent to within <0.3 ps) trigger to the sampling scope, the DAC board allows us to stroboscopically reconstruct the amplitude and phase of the microwave waveform, as described in detail in Appendix D. In turn, knowledge of this waveform allows us to provide the Python libraries with calibration parameters that correct for the DC offsets on the two ports of the transmit IQ mixer (Appendix C.2), for the amplitude and phase imbalances of the transmit IQ mixer (Appendix C.2), and for the DC offset, amplitude imbalances, and phase errors of the heterodyne detector (Appendix C.2). After an initial calibration step, this permits the Python libraries to automatically output pulse sequences and detect the free induction decay (FID) and echo signals with highly accurate amplitude and phase control.

2.2.   Samples

The experiments presented here employed one of two samples, both of which were loaded into a 3 mm i.d. 4 mm o.d. fused quartz EPR tube (Part 3x4, Technical Glass Products, Painesville Twp., OH).

Sample A: Several flakes (~1-5 mg) of a solid BDPA (α,γ-Bisdiphenylene-β-phenylallyl) complex with benzene (1:1) was used without further modification (Product 152560, Sigma Aldrich, St. Louis, MO). Both, the T_1 and T_m relaxation times for this sample are approximately 100 ns.[20]

Sample B: Following the procedure used by Maly et. al.,[20] BDPA was dissolved in toluene and then diluted in a polystyrene matrix to a concentration of 46 mmol BDPA / kg of polystyrene (Product 331651, Sigma Aldrich, St. Louis, MO). The BDPA-polystyrene-toluene paste was then dried by spreading it onto a watch glass. After sitting for 6 hours, the sample was dried under vacuum overnight for 12 hours. 28 mg of the now powdery, dilute sample were packed into the EPR tube. The T_1 relaxation time, determined by inversion recovery, was ~5 μs, and the phase memory time, T_m, determined by spin-echo measurements, was ~250 ns.

3. Results and Discussion

In this section, we present the basic performance and capabilities of the AWG X-band EPR spectrometer. First (in Sec. 3.1), we demonstrate its performance by generating microwave pulses with arbitrarily designed amplitudes and phase, and with high fidelity. Then (in Sec. 3.2), we test that it correctly applies widely used phase cycling schemes to both echo and FID data. Next (in Sec. 3.3),we demonstrate that the offset-dependent response of the spins actually responds to the shaped pulses in the expected fashion. We also test that the spectrometer can control the spacing between pulses with a resolution of ≤250ps (in Sec. 3.4), as verified both by scope captures and a finely resolved T_2 relaxation curve. Finally (in Sec. 3.5), we verify the long-term phase stability of the system by confirming that it exhibits coherent signal averaging.

3.1. Generation of Shaped Pulses

The capability of the AWG to generate shaped pulses with high fidelity, linearity, and phase stability needed to be verified. For this purpose, a variety of different pulse shapes was programmed by defining the waveform in analytical terms with an arbitrarily high resolution (Appendix B.2), automatically calibrated (Appendix C.2), subsequently down-sampled to 1 ns resolution and synthesized in the DAC board (Appendix C.1). A series of composite pulses (+x, –x, +y, –y) is the simplest example to show control over the pulse phase. A triangular pulse is used to show linearity of the system up to a maximum power. A Gaussian pulse, a sinc pulse that was truncated after the 4th side lobe, and an adiabatic rapid passage sech/tanh pulse[21,22] find frequent application in NMR experiments,should also offer significant advancements in EPR, and were thus used as examples.

The pulse sequence was captured on the sampling oscilloscope with absolute phase information after being amplified to a power of 12-13 W (41dBm) using the procedure described in Appendix D to compare the targeted waveform with the experimentally generated waveform. As shown by **Fig. 3**, all pulses were generated with high fidelity, with a root-mean-squared deviation (RMSD) of 0.081, 0.066, 0.044, 0.067, and 0.071, respectively from the target waveforms, showing excellent phase stability and linearity of the system. Slight deviations can be seen when exceeding 70% of the maximum output power of the AWG, but are negligible at lower powers.
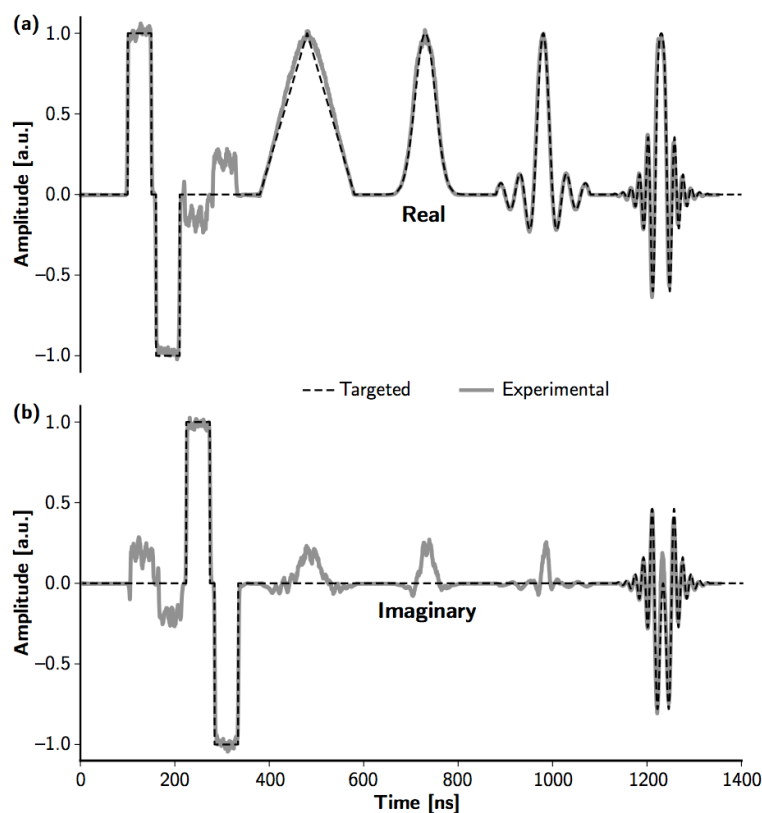
Fig. 3:Captured pulse sequence with multiple shaped pulses. Real (a) and imaginary (b) component of a targeted waveform (black dashed lines) and the microwave waveform captured on the sampling oscilloscope (grey, solid lines) following the procedures described in Appendices C.1, C.2, and D. The target waveform consists of a sequence of composite pulses, a triangular pulse, a Gaussian pulse, a truncated sinc pulse, and a sech/tanh adiabatic rapid passage (left to right, respectively).

3.2. Phase Cycling

Phase cycling is ubiquitous and essential for pulsed EPR and NMR experiments due to its ability to select signal belonging only to particular coherence transfer pathways, correct for receiver imbalances, and remove certain background signals.[23] Some applications, in particular double quantum coherence (DQC) based distance measurements,[24] demand highly accurate phase cycling. This is typically achieved by directing the microwave pulse waveform through one of several channels with pre-set phase delays, e.g. requiring 4 channels to cycle between +x, –x, +y and –y phases. However, the spectrometer we present here can implement fully functional phase cycling simply by adjusting the relative scaling in the two AWG quadrature channels that feed into the IQ mixer. This approach, termed "digital phase cycling by AWG" correctly selects coherence pathways or corrects for receiver imperfections[23,25] without the need for any pre-set phase delay channels or mechanically moving parts to define a variable phase delay. It offers a less

hardware oriented approach to phase cycling that provides superior control over achieving desired and arbitrary phase variations for each pulse, compared to the 4 possible fixed phases (+x, −x, +y, −y) of a standard commercial instrument.

Here, we present the utility and performance of our digital AWG phase cycling approach by demonstrating its impact on basic experimental tasks, such as the detection of an artifact-free echo signal. Without phase cycling, one must acquire an off-resonance "background scan" that is subtracted from the on-resonance signal. By comparison, phase cycling can improve the signal-to-noise ratio by a factor of 2, since it can remove residual pulse ring-down from the echo signal, while detecting on resonance signal at all times. This is possible because the ring-down of a π pulse maintains the same phase as the pulse throughout the phase cycle, while the spin echo adapts a variety of different phases,[26] as shown in **Table 1**. Thus, the 16-step phase cycle that selects the coherence transfer pathway of the echo (**Fig. 4(b)**) removes any pulse ring-down as well as any residual FID signal (which traverses a different coherence pathway).

$\pi/2$ pulse phase	π pulse phase	receiverphase
+x	+x	+y
+y	+x	+x
−x	+x	−y
−y	+x	−x
+x	+y	−y
+y	+y	−x
−x	+y	+y
−y	+y	+x
+x	−x	+y
+y	−x	+x
−x	−x	−y
−y	−x	−x
+x	−y	−y
+y	−y	−x
−x	−y	+y
−y	−y	+x

Table 1:16-step phase cycle. The table shows the phases of the $\pi/2$ and π pulse as well as the receiver phase to detect the spin echo signal.

To illustrate the projected SNR improvement using phase cycling and the high precision and stability of the pulse phase, a Hahn echo sequence (**Fig. 4(a)**), with a 60 ns $\pi/2$-pulse and a 120 ns π-pulse, was used to acquire signal from Sample B. The resonator was over-coupled to a Q of 1,000and the phase of the pulses and receiver were cycled according to the 16-phase cycle shown in **Table 1**. As expected and shown by **Fig. 4(c)**, both phase cycling and background subtraction yield clean, identical echoes, while the SNR of the phase cycled result is approximately twice as large when the same number of total scans are acquired with both methods.
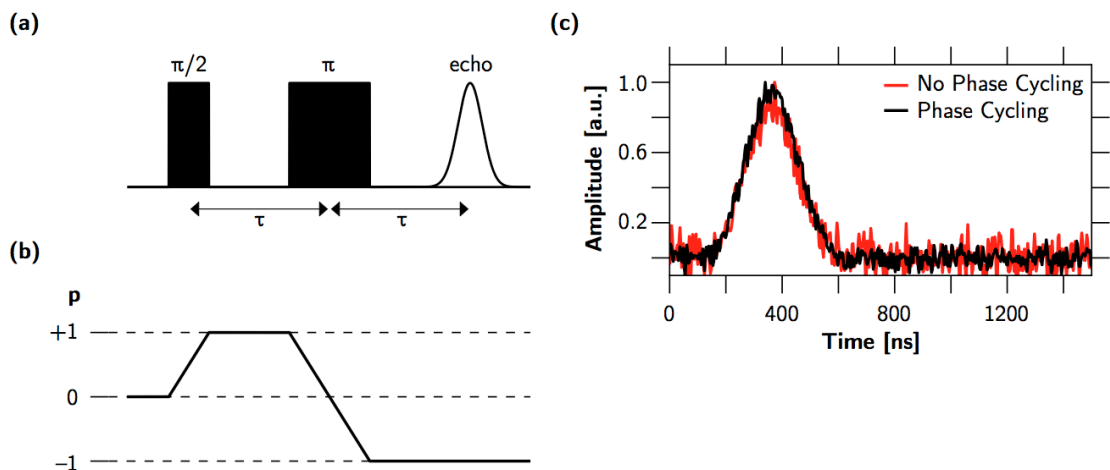
Fig. 4:Hahn echo measurement to show how phase cycling improves the SNR. Hahn echo pulse sequence (a) and respective coherence transfer pathway (b), as well as SNR comparison (c) between off-resonance background subtraction (red) and 16-step phase cycle (black) for a Hahn echo measurementaccording to (a) and Table 1. A 400 MHz digital band-pass filter was applied. The SNR (integrated echo intensity vs. RMSD of the noise) is 9.6 for off-resonance background subtraction and 18.4 for phase cycling.

In the case where we are collecting an FID, phase cycling no longer offers the same advantage in removing the ring-down from the signal, however, we can still employ phase cycling to eliminate instrumental imperfections, an example of which is the receiver imbalance. If the two quadrature detection channels are not precisely 90° out of phase with each other or have different sensitivities, a negative frequency mirror peak appears in the Fourier-transform of the FID.[27] As shown in **Fig. 5**, when an FID signal is acquired with a 4-step phase cycle, the phase cycling provided by the spectrometer removes the artifactual mirror peak that occurs in the Fourier-transform of the FID. The complete elimination of the mirror peak to within the noise of the spectrometer demonstrates the precision and stability of the AWG digital phase cycling method without the need for separate pre-set phase delay channels.
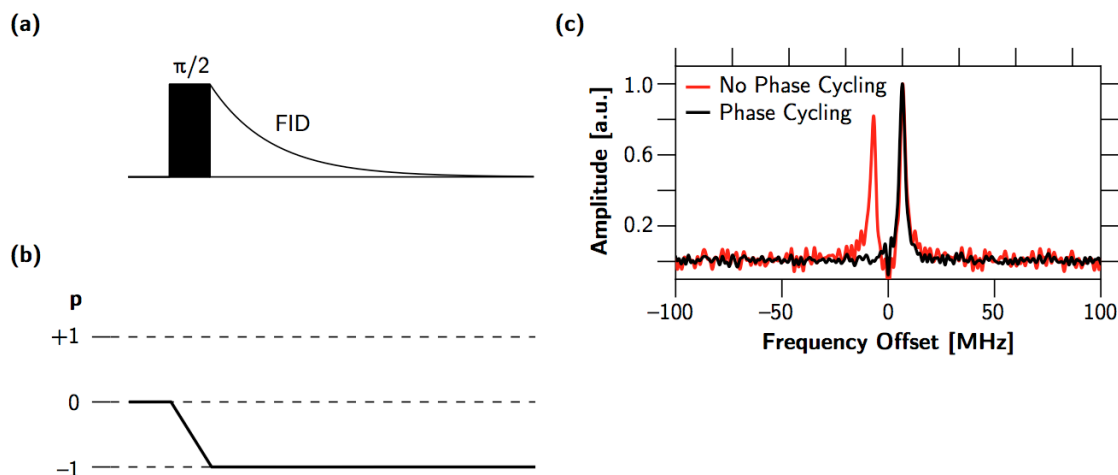
(a)

π/2

FID

(b)

p

+1

0

−1

(c)

Amplitude [a.u.]

No Phase Cycling
Phase Cycling

1.0

0.6

0.2

−100   −50   0   50   100

Frequency Offset [MHz]

Fig. 5:FID measurement to show how phase cycling corrects for receiver imbalances.FID pulse sequence (a) and respective coherence transfer pathway (b). Fourier-transform of FID with magnetic field set 2.4 G off-resonance. The negative frequency peak due to receiver imbalances can be completely eliminated with a 4-step phase cycle (+x, +y, −x, −y).

3.3.   Spin Response to Arbitrarily Shaped Pulses

In pulsed EPR, there are many situations where one is limited by "hard" square pulses. Optimized pulses have been shown to have many advantages in NMR, but, except in very few specialized laboratories, optimized pulse shapes have not been fully exploited for EPR, given the lack of AWG capabilities for pulsed X-band EPR. The AWG capabilities of the spectrometer presented here allow us to generate any arbitrary pulse shape; however, the microwave components (i.e. waveguides) and the resonator will have some effect on the pulse shape which will become increasingly relevant at higher resonator Q. By monitoring the spin response from a narrow line as a function of field, we can acquire the frequency profile of an arbitrary pulse to verify that the spins actually respond in the predicted fashion.

We have, therefore, chosen three pulse types in order to validate that the correct pulse shape is not only generated by the AWG, but also arrives at the sample within the resonator. A sample with a narrow EPR line (Sample A) mapped out the excitation profile of a square, a truncated sinc, and a Gaussian pulse by sweeping the external magnetic field. By using small tip angles, i.e. remaining within the linear response limit, we generate an excitation profile that corresponds to the Fourier transform of the excitation pulse. The magnetic field was swept over a range of ±12 G in steps of 0.25 G around the resonant magnetic field. At each field, the sample was excited with a single pulse and the FID of the sample was recorded. The FID was Fourier transformed, filtered with a 60 MHz digital bandpass filter, and the integrated amplitude was plotted against the magnetic field offset. Thus, the narrow

spectrum of the BDPA sample (FWHM = 1.4 G) selects the amplitude of a narrow spectral slice of the excitation profile of the pulse, and by sweeping the magnetic field, we can map out the entire excitation profile of the sample.

Fig. 6 shows the excitation profiles resulting from square (a), a Gaussian (b), and a truncated sinc (c) pulses, respectively. The dashed lines show the Fourier transforms of the excitation pulses used, which represent the excitation profiles of the pulses predicted by the small tip angle approximation (which is valid for these measurements), whereas the solid lines show the experimentally measured excitation profile of the spins as a function of resonance offset. The square-shaped pulse was 100 ns long. The sinc pulse with the same maximum amplitude was truncated after the 4th side lobe as shown in **Fig. 3** and had a length of 250 ns to yield a similar signal amplitude – i.e. tip angle. The Gaussian pulse was 250 ns long with a FWHM of 88 ns and also featured the same maximum amplitude and tip angle. All three excitation spectra match the expected profiles with high fidelity (RMSD 0.061, 0.053, and 0.120, respectively). The side features of the profiles are attenuated due to the limited bandwidth of the resonator; the quality factor of the resonator, Q=400, corresponds to a FWHM of 24 MHz and thus reduces the detected amplitude for larger resonance offsets.
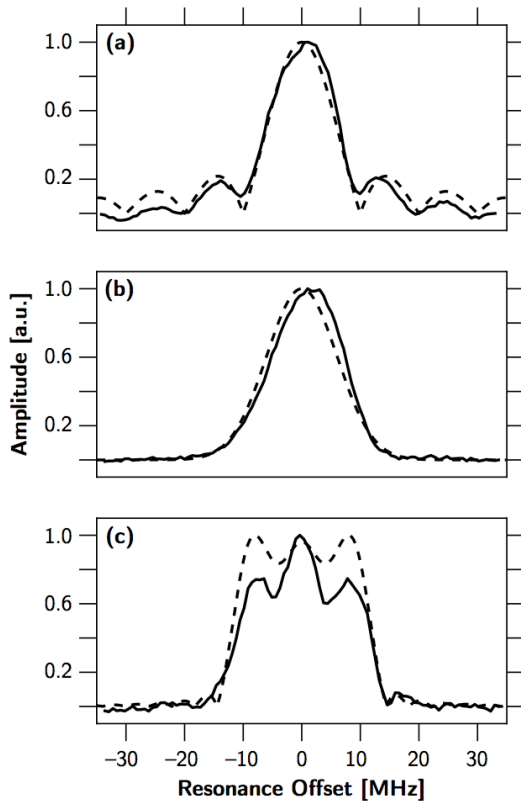

Fig. 6:Spin excitation profiles resulting from shaped pulses. Normalized spin excitation profiles (solid lines) generated by a square (a), Gaussian (b), and truncated sinc (c) pulses, acquired as described in the text, and the Fourier transforms (dashed lines) of each pulse. Since the small tip angle

approximation is valid, the Fourier transforms of the pulses represent the expected excitation profiles, whereas the side features in the measured data are attenuated due to the resonator Q factor.

3.4. Test of Pulse DelayResolution

The 1 ns time resolution of the DAC board fundamentally limits the bandwidth of the pulses in frequency space. This limits, for instance, the sharpness of the edges of the pulses. However, even in the presence of such a bandwidth limitation, delays between pulses can be defined with a time resolution that is finer than 1 ns. This can be accomplished by defining the desired waveform in analytical terms with an arbitrary resolution, such as 10 ps, and properly smoothing the waveform before reducing the bandwidth in frequency space to 1 GHz to match the 1 ns time resolution of the DAC board. This "down-sampling" procedure makes use of the large dynamic range of the DAC board, and thus only restricts the sharpness of the pulse edges, whereas the relative positions of the pulses are conserved. Specifically, this preserves the distance between the centers (or edges) of the pulses and permits the definition and generation of inter-pulse delays and pulse lengths with a resolution of better than 250 ps, as **Fig. 7** experimentally demonstrates.
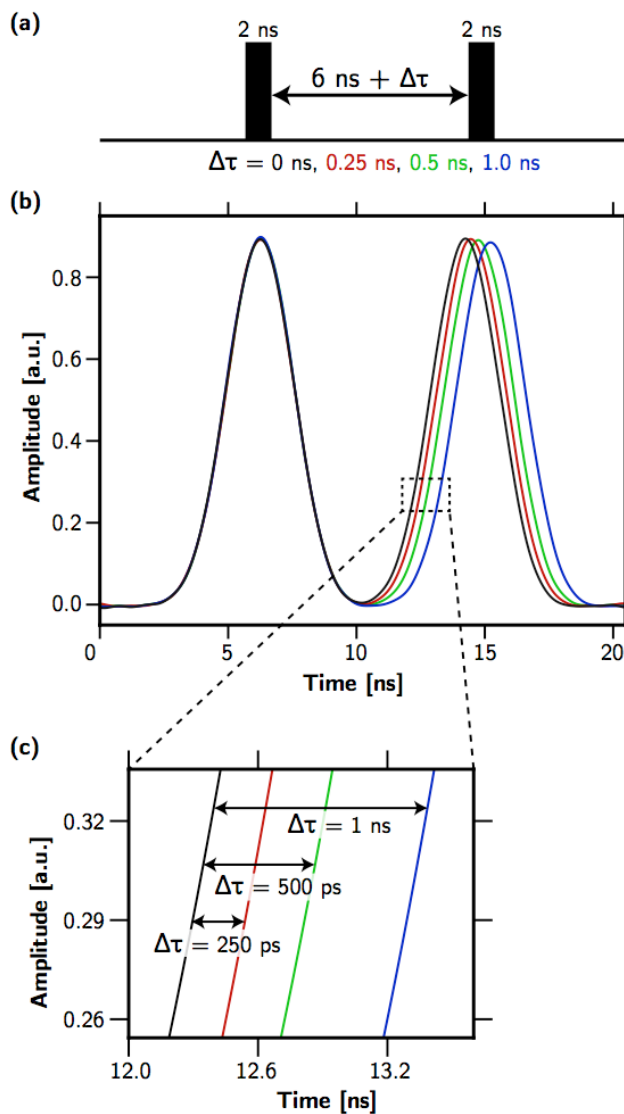
(a)

2 ns   2 ns

6 ns + Δτ

Δτ = 0 ns, 0.25 ns, 0.5 ns, 1.0 ns

(b)

Amplitude [a.u.]

Time [ns]

(c)

Amplitude [a.u.]

Δτ = 1 ns

Δτ = 500 ps

Δτ = 250 ps

Time [ns]

Fig. 7:Pulse sequence showing delays that are defined with ≤250 ps time resolution. The pulse sequence consisting of two 2 ns wide pulses with a varying pulse delay of 6 ns, 6.25 ns, 6.5 ns, and 7 ns (a) generates a microwave waveform (b), which is captured on the sampling oscilloscope (as described in Appendix D) and digitally filtered with a 1 GHz bandpass. As the higher resolution inset (c) shows, delays with ≤250 ps resolution are generated with high fidelity.

This capability allows one to determine a spin-echo relaxation decay with nearly unprecedented time resolution. This should allow one to determine T_m, and even multiple overlapping relaxation contributions, with high precision and is particularly interesting for short decay times. To demonstrate this capability, the phase-cycled Hahn echo sequence described in the previous section acquired signal from Sample A at a resonator Q of 500 and $\pi/2$ length of 60 ns. The delay time, τ,

between the $\pi/2$- and the π-pulse was varied and signal was acquired with 5,000 averages (**Fig. 8**). The best-fit exponential decay (solid line) determines the T_m relaxation time to be 245±7 ns. **Fig. 8 (inset)** shows the same measurement at a 250 ps resolution in τ. Demonstrating the spectrometer's continuous control over τ, the higher resolution data smoothly interpolates between the lower resolution points, closely following the best-fit exponential decay.
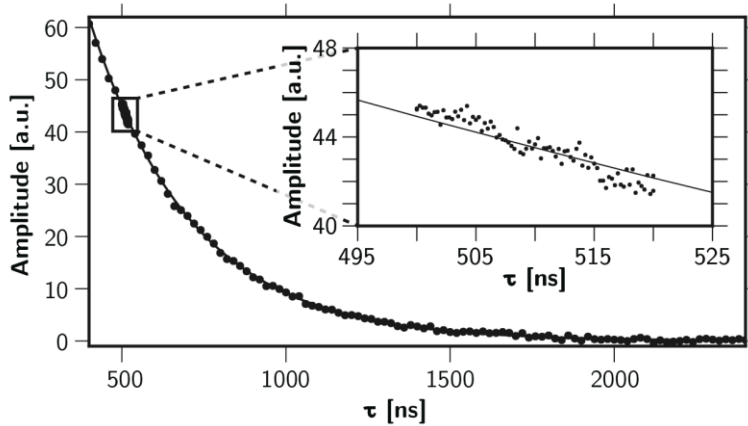

Fig. 8:T_m relaxation curve with 250 ps step size for pulse delay.T_m relaxation curve recorded via a Hahn echo sequence on Sample B.A 12 MHz digital bandpass filter was applied to the data and the echo area was integrated and plotted against the delay time, τ, between the pulses, which was varied in 34 ns steps. The solid black line (in both the main plot and inset) gives the exponential fit of this data, with T_m = 245±7 ns. The inset shows the same measurement, acquired with higher time resolution; for this data, a 250 ps step size was used for the pulse delay.

3.5. Signal Coherence Test

To show that the various hardware components remain phase coherent for an extended period of time, EPR signal was detected (on Sample A) with a varying number of averages, n. With perfect phase coherence, the SNR would scale linearly with $\sqrt{n}$. A $\pi/2$ square pulse of 60 ns length was repeated n times at a rate of 100 kHz, yielding FIDs that were signal averaged on the oscilloscope and Fourier transformed to yield a spectrum. The SNR was determined from the integrated signal peak divided by the standard deviation of the noise. The SNR was re-determined for values of n ranging from 500 to 29,500 and plotted against $\sqrt{n}$ as shown in **Fig. 9**. The linear dependence of the SNR on $\sqrt{n}$ shows that the transmitter and receiver systems maintain excellent phase coherence.
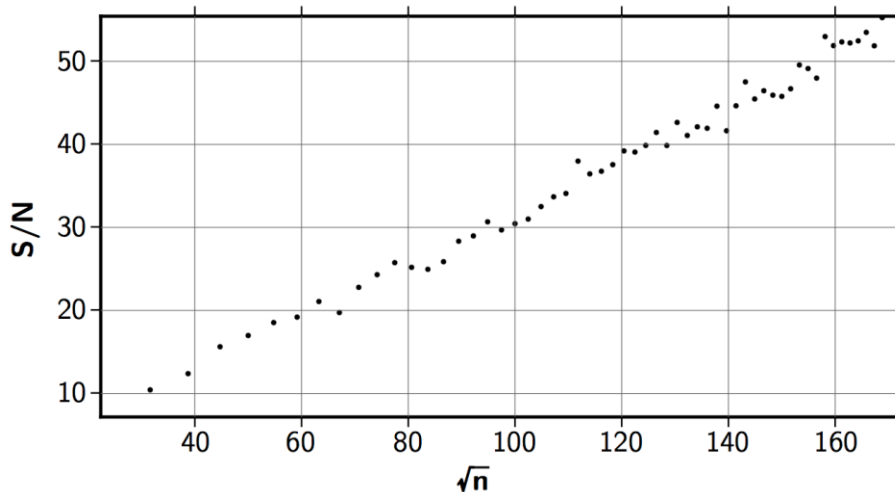
Fig. 9:Signal coherence test.SNR, calculated as explained in the text, as a function of $\sqrt{n}$, where n is the number of scans that are averaged.

4. Summary and Outlook

Initially, this project sought simply to add arbitrary waveform capabilities to X-band EPR, as the limitations of square pulses were obvious and needed to be overcome. In the process of accomplishing this goal, several interesting and new findings were made. We have presented a design strategy that employs a DAC board as the central control unit of the pulsed EPR spectrometer, and find that it dramatically decreases the complexity of the instrument. In this design, the DAC board is employed not only to shape pulses, but also to precisely control the phase and amplitude of the pulses, eliminating the need for separate pulse-forming "channels," and also to serve as a timing unit that triggers amplifiers and data acquisition devices (and, in the future, high isolation switches). This design also grants nearly arbitrary control over the inter-pulse spacing, which allows for spin relaxation time measurements with unprecedented time resolution.

We find that a design based on mixing a shaped intermediate frequency wave with a higher frequency carrier proves to be extremely versatile. In particular, the carrier frequency can be changed without the need to recalculate the entire waveform. Furthermore, with the Python programming platform presented here, arbitrary waveforms can be calculated from analytical descriptions on the fly, which also sets this development apart from commercially available arbitrary waveform generators. This setup could be directly adapted to several other frequency bands, including K-band (18-26.5 GHz) and Q-band (33-50 GHz), simply by replacing the X-band-specific components (the microwave source, mixer, and the microwave resonator and bridge components). The only limitation for applying the same AWG technology to much higher frequencies is that the intrinsic 1 GHz bandwidth would no longer cover the bandwidth of the resonator; however commercial DAC boards that operate at higher bandwidths are already available, and, with effort, the design

of the present DAC board could be scaled to a faster sampling rate and subsequently higher bandwidth. However, most importantly, at X-band this spectrometer design can successfully control the excitation profiles of the spins – in fact, these match the theoretical profiles with fidelity beyond our expectations and promise significant improvements for EPR measurement techniques. Optimization procedures and active feedback techniques can be implemented in this design to further improve the excitation profiles.

Wider excitation bandwidths as well as sharper excitation profiles, both of which are specifications that this spectrometer design can provide directly, would directly benefit prominent pulsed EPR measurements for biological applications, such as DEER. This spectrometer can precisely control the amplitude and phase of a pulse lasting for several ns, which is exactly the capability that one would need to directly apply standard algorithms from NMR in order to generate sharper spectral slices.[9] In order to increase the excitation bandwidth of a pulse, rather than increasing the pulse amplitude up to technical limitations, shaped pulses such as adiabatic rapid passages[22,28] or Frank sequences[29,30] can provide broadband excitation, even with limited microwave power. In addition, double quantum coherence (DQC) experiments can be significantly improved with shaped pulses, since the task of transferring into a double-quantum state is greatly improved with the use of optimized arbitrarily shaped pulses[10].

The spectrometer is at the same time both easy to control and highly customizable. It can be controlled in a versatile and user-friendly system, thanks to the open-source, Python-based programming platform. This platform seamlessly interfaces not just to the central DAC board, but to a variety of hardware components with any type of communication protocol. Diverse customizations to the user's needs can be implemented around the centralized hardware and software design of this spectrometer. These customizations include the option to integrate the AWG into commercially available EPR spectrometers, which offer the advantage of being equipped with high-quality microwave switches to close off the high-power amplifiers and significantly improve the SNR. Furthermore, commercial instruments offer intuitive graphical user interfaces that users are accustomed to using for production runs of EPR experiments and that include an assortment of post-processing routines.

The spectrometer we have developed here does not only overcome the limitations of square pulses by enabling arbitrary waveform capabilities for pulsed EPR, but also presents an alternative approach to spectrometer design. By combining the functionalities of controlling phase and amplitude of the pulses, as well as the timing of all spectrometer components, into one digital control unit, this system offers significant advantages over the present state-of-the-art for pulsed EPR spectrometers.

Acknowledgements

Appendix A: Hardware

A.1.   Magnet and Microwave Source

A schematic overview of the spectrometer is shown in **Fig. 1** in the main text. A field controller (Bruker ER 032 M) controls the 0.35 T static field generated by the electromagnet (Bruker ER 070, Fig. 1 – #1). A YIG-tuned oscillator (MicroLambda MLSL-1178, Fig. 1 – #2) generates a low-phase-noise (–53 dBc/Hz at 100 Hz offset, –60 dBc/Hz at 1 kHz offset, –93 dBc/Hz at 10 kHz offset) +10 dBmcw X-band sine wave, which is split, with one channel pre-amplified (MiniCircuits ZX60-183+, Fig. 1 – #3) to 18 dBm and fed into the home-built AWG unit (**Fig. 2**) and the other channel sent to the heterodyne receiver (Section A.4). Communication with the field controller occurs through a GPIB connection; a GPIB-Ethernet Controller 1.2 by Prologix, LLC allows the Python library to communicate with this and all other GPIB devices through a TCP/IP socket. The microwave source is computer controlled with a USB interface (FTDI FT245R embedded in the UM245R development board) together with the FTDI D2XX drivers that allow direct access to the device in the "bit-bang" mode, which permits one to set the voltage levels on the various pins simultaneously. Both the static field and microwave frequency can be set from a Python script,which can also read out the current Hall probe reading and whether or not the microwave source is currently phase-locked.

A.2.   AWG Unit

The AWG unit is comprised of a two-channel 1 GHz DAC board (High Speed Circuit Consultants, software build 10, Fig. 1 – #4),[19] four Gaussian filters (High Speed Circuit Consultants) that reduce output noise, two differential amplifiers (Fig. 1 – #5) that drive the I and Q channels of an IQ mixer (Marki Microwave IQ-0618, Fig. 1 – #6), a low pass filter (Marki Microwave FLP-1250, Fig. 1 – #7) that suppresses harmonics generated by the IQ mixer, and a directional coupler (Fig. 1 – #8) that allows monitoring of the shaped microwave output of the AWG unit with 10 dB of attenuationon a sampling oscilloscope (Tektronix 11801C, Fig. 1 – #9) with two sampling heads (Tektronix SD 24, Tektronix SD 22), as described in Appendix D. Additionally, each of the two differential amplifiers has a secondary output that can be monitored on a standard digital storage oscilloscope.

The DAC board was developed by John Martinis at UCSB[19] in collaboration with Steve Waltman (High Speed Circuit Consultants), and features two differential (i.e. two port) outputs with a 14 bit (i.e. 42 dB) dynamic range and 1 ns time resolution. The memory of the board allows for storage of up to 16 μs long waveforms. Additionally, parts of the pulse sequence can be called independently and delays of arbitrary lengths can be inserted. The bandwidth limitation of the AWG unit is set by the I and Q inputs of the IQ mixer, which feature a bandwidth of 500 MHz and thus make the IQ mixer the bandwidth limiting component in the setup. A significant advantage over commercially available AWGs is that the DAC board provides four differential ECL trigger outputs that can be utilized to control other

components of the spectrometer. For this spectrometer, an ECL-to-TTL converter was built (ON Semiconductor ECLSOIC8EVB and MC100ELT21) to open and close the gate of a TWT amplifier. Another ECL trigger output triggers the sampling oscilloscope as well as the oscilloscope connected to the heterodyne receiver. Thus, the DAC board not only controls the phase and shape of the microwave pulses, but also functions as the central timing unit. The FPGA-based design of the DAC board also allows for custom modifications of the its functionality, if desired.

A.3.   Microwave Transmission

The shaped pulse output of the AWG, approximately –10 dBm coming out of the mixer, is pre-amplified (MiniCircuits ZX60-183+) by 24 dB and further amplified (Fig. 1 – #10) by either a 1 kW traveling wave tube (TWT) amplifier (Applied Systems Engineering Model 117), which we measured to have a gain of 60 dB and a P1dB of 61 dBm, or an array of four solid-state amplifiers. The four amplifiers (Advanced Microwave PA2803-24) each yield a gain of 30 dB (P1dB 35 dBm each) and are adjusted with phase shifters to yield coherent outputs that are combined for a net gain of 36 dB to reach a maximum power of approximately 12-13 W of power (41 dBm). Specifically, the array of solid-state amplifiers uses 3 splitters (MiniCircuits ZX10-2-126) to divide the signal into 4 pathways, 3 phase shifters (AeroflexWeinschel980-4) to adjust the phase of 3 of the pathways to match the first one, before the signal is fed into the 4 amplifiers, and 4 isolators (UTE Microwave, CT-5450-OT) to protect the amplifier outputs from reflections before the 4 pathways are combined (Narda Microwave 4326-4) again. The amplifiers are powered by a linear power supply (Protek 18020M), mounted on a thick aluminum block and additionally cooled by computer fans. A 4-port circulator, with port 4 terminated (Cascade Research X-43-2, Fig. 1 – #11), directs the microwave pulses to the resonator (Bruker ER4118X-MD5, Fig 1. – #12) that holds the sample and returns the reflected signal to the detector.
For the purposes of monitoring the system, a directional coupler (Fig. 1 – #13) directs –20 dB of reflected signal to the sampling oscilloscope. A second directional coupler, placed in front of the YIG-tuned source (Fig. 1 – #2), directs –20 dB of the X-band carrier wave to the second channel of the sampling oscilloscope, where it is used as a reference to determine the reflected microwave signal with absolute phase information as outlined in Appendix D.

A.4.   Microwave Detection

The microwave signal returning from the resonator is sent to a 3-port circulator (Cascade Research X43-10-1, Fig. 1 – #14) and from there to a PIN-diode limiter (Aeroflex ACLM-4571FC31K, Fig. 1 – #15), which protects the low-noise amplifier (Miteq AMF-3F-09001000-13-8P-L-HS, Fig. 1 – #16) from damage due to high power microwaves. The aforementioned circulator (Fig. 1 – #14) directs any microwave power reflected from the limiter into a high-power terminator (Fig. 1 – #17).

To obtain heterodyne detection, the amplified signal and the output of the microwave carrier are input into another IQ mixer (Marki Microwave IQ-0618, Fig. 1 – #18), generating two IF (i.e. intermediate frequency) signals in quadrature, which have a frequency range between DC and 500 MHz. These signals are amplified by two amplifiers (MiniCircuits ZFL-500+, Fig. 1 – #19) and detected with a (time-base) digital storage oscilloscope (Agilent Technologies MSO7104B, Fig. 1 – #20) or a high speed digitizer card (Agilent Acqiris 1082A).

A.5. Phase Coherence

The storage oscilloscope, the digitizer card, the YIG source, and the DAC board all contain phase locked loops (PLLs) locked to an oven-controlled 10 MHz reference oscillator (Electronic Research Co. Model 130, Fig. 1 – #21) that is connected to a distribution amplifier (Stanford Research Systems Model FS735, Fig. 1 – #22).

A.6. Pickup Coil

A pickup coil is implemented to observe a close approximation of the pulse shape inside the cavity and could be used to determine the necessary corrections to a pulse shape to match the desired waveform as closely as possible.[14]Thepickup coil (Fig. 1 – #23) is made by soldering the inner wire of a semi-rigid cable (RG402/U) to its outer shielding to create a small loop. A low-noise amplifier (MiniCircuits ZVA-183+, Fig. 1 – #24) connected to the pickup coil amplifies the signal from the pickup coil to a reasonable amplitude and is protected against reflections by an isolator (MECA Electronics CS-10.200) that is connected to its output. The signal is detected with absolute phase information on an additional channel of the sampling oscilloscope. This design has not been used for the measurements presented, but offers opportunity for future developments.

Appendix B: DAC Board Control Software

B.1.   DAC Board Communication

To control the DAC board from a Python platform, the following software is needed:
- LabRAD Manager
- LabRAD Direct Ethernet Server
- LabRAD GHz FPGA Server
- LabRAD Registry Editor
- Python 2.6 or 2.7
- Pylabrad
- Pyreadline
- Pywin32
- SciPy
- Twisted (www.twistedmatrix.com)
- Numpy
- iPython
- Matplotlib

The LabRAD components, basic scripts to run and control the DAC board as well as an initial set of registry keys for the LabRAD registry can be acquired by contacting the authors. To simplify the procedure of using the DAC board, the following environmental variables should be set:
- LabRADHost = localhost
- LabRADNode = EPR
- LabRADPassword = password
- LabRADPort = 7682

The HDL code used for the DAC board FPGA was version 10, as developed by John Martinis.[17] The Python scripts used to communicate with the DAC board are in-house software extensively modified from developments by Daniel Sank from the Martinis group, and can be acquired by contacting the authors.

B.2.   Waveform Generation

The Python scripts that communicate with the DAC board allow arbitrary waveforms to be generated on-the-fly. These can be based on analytical descriptions or specified with arbitrary time resolution. **Fig. B1** shows an example: this pulse sequence generates the waveform shown in **Fig. 3** (Section 3.1).

The function "`make_highres_waveform(list, resolution)`" can be called with a list of tuples that define (1) the type of pulse, (2) the phase of the pulse, and (3) the length of the pulse or delay. The first parameter can be `"rect"` (rectangular pulse), `"delay"`, or `"function"` (defined by a function – here a lambda (i.e. inline) function giving an analytical expression for the pulse waveform).

A rectangular pulse uses the second argument to define the pulse phase, which can be either "x", "y", "-x", "-y" or any angle between 0 and 360 degrees (**Fig. B1**, lines 2 and 3). The third parameter defines the length of a pulse in units of seconds. In case of a delay, the second parameter defines its length. If the pulse type "function" is chosen, the second parameter is a function that define the pulse shape as a function of time; here we employ lambda (inline) functions to generate analytically described functions that can be edited on-the-fly. **Fig. B1** shows a triangular pulse (line 5), a Gaussian pulse (line 7), a truncated sinc pulse (line 9) and an adiabatic rapid passage sech/tanh pulse (line 11) as examples. The parameter "resolution" defines the time resolution for the pulse sequence – 40 ps in this case – that can be arbitrarily chosen.

The function "digitize(wave)" (line 14) takes the desired waveform as an argument, filters it with a 1 GHz Gaussian band-pass and down-samples it to a 1 ns time resolution. The previously acquired calibration parameters (Appendix C.2) and transfer function calibration (Appendix C.3) are applied, the waveform is translated into commands for the DAC board, transferred to the DAC board, and synthesized as described in Appendix C.1 (**Table C1**, lines 2 to 7).

```
1   wave = p.make_highres_waveform([
2       ('rect','x',50e-9),('delay',10e-9),('rect','-x',50e-9),('delay',10e-9),
3       ('rect','y',50e-9),('delay',10e-9),('rect','-y',50e-9),
4       ('delay',50e-9),
5       ('function', lambda x: (1-x)/2,100e-9),('function', lambda x: (x+1)/2,100e-9),
6       ('delay',50e-9),
7       ('function', lambda x: exp(-(x/0.3)**2),200e-9),
8       ('delay',50e-9),
9       ('function', lambda x: sin(x*5*pi+200e-9)/(x*5*pi+200e-9),200e-9),
10      ('delay',50e-9),
11      ('function',lambda x: sech(6*x)**(1+6j),200e-9)
12      ],resolution = 4e-11)
13
14  p.digitize(wave)
```

> **Fig. B1:** Code that generates a pulse sequence -- in this case a composite pulse comprising 4 rectangular pulses of different phases: a triangular pulse, a Gaussian pulse, a truncated sinc pulse, and an adiabatic rapid passage sech/tanh pulse.

The language for pulse programming was kept simple to maximize user-friendliness. Arbitrary pulse shapes can be generated within a fraction of a second, and simple loops can be set up to perform two dimensional experiments, such as the T_2 experiment presented in Sec. 3.4 and the coherence test in Sec. 3.5.

Appendix C: Digitization and Synthesizer Calibration

Descriptions of the algorithms used to generate, capture, as well as correct and calibrate arbitrary waveforms are given in this appendix.

C.1.   Digitization and Waveform Generation

To digitize and generate an arbitrary waveform with the AWG from analytical descriptions, the desired waveform is defined with arbitrary length and resolution, then filtered with a 1 GHz Gaussian bandpass filter and down-sampled to a 1 ns time resolution to match the resolution of the DAC board. The IQ mixer calibration (Appendix C.2) as well as the transfer function calibration (Appendix C.3) are applied to take hardware imperfections into account and match the desired waveform as closely as possible. Subsequently, the waveform is translated into commands for the DAC board and transferred to the system. **Table C1** describes this procedure.

1. Define a desired waveform of arbitrary length and resolution $w(t)$

2. Filter with 1 GHz Gaussian: $w(t) \otimes e^{-\left(\frac{x}{1\,\text{ns}}\right)^2}$

3. Reduce bandwidth to 1 GHz:

   $w_i = \int_0^\infty w(t)\delta(t - t_i)\mathrm{dt}$ for t_i in 1 ns, 2 ns, ..., pulselength

4. Apply IQ mixer calibration

5. Apply transfer function correction

6. Translate w_i to DAC board commands

7. Transfer waveform to DAC board

> **Table C1:** Procedure to digitize, correct, and synthesize a waveform with the AWG. The symbol "$\otimes$" indicates time-domain convolution.

C.2.   IQ Mixer Calibration

The IQ mixer used for waveform synthesis exhibits three correctable imperfections:
1. An amplitude imbalance between the two channels, i.e. "parity imbalance."
2. The phase angle between the two channels is not necessarily 90 degrees.
3. Microwave leakage occurs when no voltage is applied to both channels.

To correct for all three of these issues, a plane wave U_{in} is generated via the DAC board, mixed with the reference oscillator via the IQ mixer, and the output waveform U_{out} is captured on the sampling oscilloscope. In general, where an input waveform, U_{in}, has the form

$$U_{in}(t) = \rho_{in}(t)e^{i\phi_{in}(t)} \tag{1}$$

where ρ_{in} and ϕ_{in} are real numbers giving, respectively, the amplitude and phase modulation of the waveform, the amplitude and phase of the output waveform will be altered according to equations

$$\Re[U_{out}(t)] = (1 + B_\Re)A_\Re\rho_{in}(t)\cos[\phi_{in}(t) + \vartheta_\Re] + C_\Re \tag{2}$$

$$\Im[U_{out}(t)] = (1 + B_\Im)A_\Im\rho_{in}(t)\cos[\phi_{in}(t) + \vartheta_\Im] + C_\Im \tag{3}$$

as a result of these imperfections.[29] The A_R and A_I represent the output parity imbalance, the B_R and B_I represent the input parity imbalance, the ϑ_R and ϑ_I denote a phase shift (arising from slightly different path lengths in each channel), and the C_R and C_I represent the DC offset of the real (eq. 2) and imaginary (eq. 3) components of the output waveform.
Specifically, after outputting a plane-wave U_{out}, the real and imaginary components of the output waveform, which is captured on the sampling scope, are fit to equations (eq. 2) and (eq. 3), respectively, as a function of the input phase.

Once these calibration parameter have been determined, one can solve eq. 2 and eq. 1 with a standard zero-finding algorithm to determine the input values of ρ_{in} and ϕ_{in} needed to yield any desired output amplitude and phase (i.e. $|U_{out}|$ and angle(U_{out})), respectively. This corrects the amplitude and phase of the output waveform. In particular, the microwave leakage is corrected by subtracting the terms C_R and C_I from the input waveform's real and imaginary components, respectively. This applies a voltage to each channel of the mixer to minimize microwave leakage at the output and allows for an isolation of more than 50 dB post amplification.

The IQ mixer used for detection exhibits the same issues as the mixer used for waveform synthesis.Therefore, an analogous calibration procedure can be applied, the difference being that non-linearities are accounted for in post processing.

C.3.   Transfer Function Calibration

To maximize the fidelity with which pulses are generated, the transfer function of the spectrometer can be taken into account as a final step by capturing the generated waveform and comparing it to the desired pulse shape. Linear response theory states that the output waveform, $p_{out}(t)$, can be described as a convolution of the input waveform, $p_{in}(t)$, with the impulse response of the system – i.e. the inverse Fourier transform of the transfer function, $T(f)$, of the system. We represent this as

$$p_{out}(t) = p_{in}(t) \otimes \mathcal{F}^{-1}\{T(f)\}(t) \tag{4}$$

where $F^{-1}\{...\}$ represents the Fourier transform and $\otimes$ again represents a time-domain covolution. After Fourier transformation, the transfer function in frequency space can be found, following from

$$\mathcal{F}\{p_{out}(t)\}(f) = \mathcal{F}\{p_{in}(t)\}(f)T(f) \tag{5}$$

The transfer function, $T(f)$, can be subsequently applied to the initial waveform function to generate the desired waveform $p_{cor}(t)$ as described in **Table C2**.

Instead of using the desired output pulse to determine the transfer function, a 1 ns square pulse on each DAC channel can be used to determine the impulse response function of the spectrometer and the transfer functions for both channels T_A (corresponding to a real 1 ns pulse) and T_B (corresponding to an imaginary 1 ns pulse) are added to determine the total transfer function T. The procedure is described in **Table C2**. This procedure was not utilized in the experiments presented, but offers opportunity for future applications.

1. Generate 1 ns square pulse $p_{in}(t)$ on DAC channel A and capture impulse response $p_{out}(t)$ on sampling oscilloscope.

2. Fourier transform the generated waveform to yield

    $\mathcal{F}\{(p_{in}(t)\}(f)$ and the impulse response to yield

    $\mathcal{F}\{(p_{out}(t)\}(f)$.

3. Find transfer function $T_A(f) = \frac{\mathcal{F}\{p_{out}(t)\}(f)}{\mathcal{F}\{p_{in}(t)\}(f)}$

4. Repeat steps 1 through 3 with DAC channel B to find total transfer function $T(f) = T_A(f) + T_B(f)$

5. Find Fourier transform of corrected output waveform

    $\mathcal{F}\{p_{cor}(t)\}(f) = \frac{\mathcal{F}\{p_{in}(t)\}(f)}{T(f)}$

6. Inverse Fourier transform corrected output waveform to yield

    $\mathcal{F}^{-1}\{\mathcal{F}\{p_{cor}(t)\}(f)\}(t) = p_{cor}(t)$.

Table C2: Procedure to capture the transfer function of the spectrometer and apply the correction to an arbitrary waveform to match the desired waveform as closely as possible.

Appendix D: Waveform Capturing

To be able to generate arbitrary waveforms with a defined phase, the absolute phase of the generated pulse needs to be determined, so that a calibration procedure can be applied. Any microwave pulse or reflection of the resonator in the system can be detected with absolute phase information by employing the second channel of the sampling oscilloscope, which is fed with the attenuated output of the microwave source. The phase of each data point of the signal channel is compared to the phase of the constant amplitude reference wave. The procedure is described in **Table D1**, where H gives the Heaviside step function ($H(x) = 1$ for $x > 0$ and $H(x) = 0$ for $x < 0$).

1. Simultaneously capture plain microwave carrier $c_{ref}(t)$ and waveform to be analyzed $c_{cap}(t)$

2. Generate analytic signal and apply bandpass filter to reduce noise:

$$\mathcal{F}\left\{c_{ref}(t)\right\}(f) := \mathcal{H}(f)\mathcal{H}(f - 10\,\text{GHz})\mathcal{F}\left\{c_{ref}(t)\right\}(f),$$

$$\mathcal{F}\left\{c_{cap}(t)\right\}(f) := \mathcal{H}(f)\mathcal{H}(f - 10\,\text{GHz})\mathcal{F}\left\{c_{cap}(t)\right\}(f)$$

with $\mathcal{F}\left\{\ldots\right\} := \int_{-\infty}^{\infty} e^{i2\pi ft}\ldots\mathrm{dt}$

3. Determine absolute phase: $c_{cap,\phi}(t) = c_{cap}(t)\dfrac{|c_{ref}(t)|}{c_{ref}(t)}$

4. Apply bandpass filter to reduce noise:

$$\mathcal{F}\left\{c_{cap,\phi}(t)\right\}(f) := \mathcal{H}(f)\mathcal{H}(f - 2\,\text{GHz})\mathcal{F}\left\{c_{cap,\phi}(t)\right\}(f)$$

Table D1: Procedure to capture a microwave waveform on the sampling oscilloscope with absolute phase information.

References

(1)   Schiemann, O.; Prisner, T. F. *Quarterly Reviews of Biophysics***2007**, *40*, 1.

(2)   Fajer, P. *Encyclopedia of Analytical Chemistry***2006**, 5725.

(3)   Jeschke, G. *ChemPhysChem***2002**, *3*, 927.

(4)   Kevan, L., Kisper, L.D. *Electron Spin Double Resonance Spectroscopy*; Interscience: New York, NY, 1976.

(5)   Hyde, J.; Chien, J.; Freed, J. *The Journal of Chemical Physics***1968**, *48*.

(6)   Swamy, M. J.; Ciani, L.; Ge, M.; Smith, A. K.; Holowka, D.; Baird, B.; Freed, J. H. *Biophysical Journal***2006**, *90*, 4452.

(7)   Chiang, Y.-W.; Costa-Filho, A. J.; Baird, B.; Freed, J. H. *The Journal of Physical Chemistry B***2011**, *115*, 10462.

(8)   Skinner, T. E.; Kobzar, K.; Luy, B.; Bendall, M. R.; Bermel, W.; Khaneja, N.; Glaser, S. J. *Journal of magnetic resonance***2006**, *179*, 241.

(9)   Pauly, J.; Le Roux, P.; Nishimura, D.; Macovski, a. *IEEE transactions on medical imaging***1991**, *10*, 53.

(10)   Khaneja, N.; Reiss, T.; Kehlet, C.; Schulte-Herbrüggen, T.; Glaser, S. J. *Journal of magnetic resonance***2005**, *172*, 296.

(11)   Crepeau, R.; Dulic, A.; Gorcester, J.; Saarinen, T.; Freed, J. *Journal of magnetic resonance***1989**, *84*, 184.

(12)   Pursley, R. H.; Kakareka, J.; Salem, G.; Devasahayam, N.; Subramanian, S.; Tschudin, R. G.; Krishna, M. C.; Pohida, T. J. *Journal of magnetic resonance***2003**, *162*, 35.

(13)   Devasahayam, N.; Murugesan, R.; Matsumoto, K.; Mitchell, J. B.; Cook, J. a.; Subramanian, S.; Krishna, M. C. *Journal of magnetic resonance***2004**, *168*, 110.

(14)   Spindler, P. E.; Zhang, Y.; Endeward, B.; Gershernzon, N.; Skinner, T. E.; Glaser, S. J.; Prisner, T. F. *Journal of magnetic resonance***2012**, *218*, 49.

(15)   Shim, J. H.; Niemeyer, I.; Zhang, J.; Suter, D. *EPL (Europhysics Letters)***2012**, *99*, 40004.

(16)   Borneman, T. W.; Cory, D. G. *Journal of magnetic resonance***2012**, *225*, 120.

(17)   Tseitlin, M.; Quine, R. W.; Rinard, G. a.; Eaton, S. S.; Eaton, G. R. *Journal of magnetic resonance***2011**, *213*, 119.

(18)   Rinard, G. a.; Quine, R. W.; Song, R.; Eaton, G. R.; Eaton, S. S. *Journal of magnetic resonance***1999**, *140*, 69.

(19)   Martinis, J. M. *Quantum Information Processing***2009**, *8*, 81.

(20)   Maly, T.; MacMillan, F.; Zwicker, K.; Kashani-Poor, N.; Brandt, U.; Prisner, T. F. *Biochemistry***2004**, *43*, 3969.

(21)   Tannús, a.; Garwood, M. *NMR in Biomedicine***1997**, *10*, 423.

(22)   Garwood, M.; DelaBarre, L. *Journal of magnetic resonance***2001**, *153*, 155.

(23)   Cavanagh, J., Fairborther, W. J., Palmer, A. G., Skelton, N. J., Rance, M. *Protein NMR Spectroscopy, Second Edition: Principles and Practice*; Academic Press: Waltham, MA, 2006.

(24)   Saxena, S.; Freed, J. H. *The Journal of Chemical Physics***1997**, *107*, 1317.

(25)   Gemperle, C.; Aebli, G.; Schweiger, A.; Chemie, P. *Journal of magnetic resonance***1990**, *256*, 241.

(26)   Keeler, J. *Understanding NMR Spectroscopy*; John Wiley & Sons Ltd.: Chinchester, England, 2005.

(27)   Stejskal, E.; Schaefer, J. *Journal of magnetic resonance***1974**, *14*, 160.

(28)   Silver, M.; Joseph, R.; Hoult, D. *Physical Review A***1985**, *31*, 2753.

(29)   Tseitlin, M.; Quine, R. W.; Eaton, S. S.; Eaton, G. R.; Halpern, H. J.; Ardenkjaer-Larsen, J.-H. *Journal of magnetic resonance***2011**, *209*, 306.

(30)   Blümich, B.; Gong, Q.; Byrne, E.; Greferath, M. *Journal of magnetic resonance***2009**, *199*, 18.

(31)   Sabah, S.; Berlin, T. U.; Lorenz, R.; Zeuthen, D. *Proceedings of the European Particle Accelerator Conference 1998, Sweden***1998**, 1589.